Research Article

Journal of the Optical Society of America A

OPTICS, IMAGE SCIENCE, AND VISION

High étendue Fourier transform spectroscopy by quadratic off-axis path difference error cancellation

Selene Amy Routley,[1,2,*] Jamie Flynn,[2] Antony Martin,[2] and William Palmer[2]

[1]Deutsches Zentrum für Luft- und Raumfahrt, Rutherfordstraße 2, 12489 Berlin Adlershof, Berlin, Germany
[2]Hone Ag Pty. Ltd., Suite 65, Level 2, 113-145 Hunter St, Newcastle, NSW 2300, Australia
*Corresponding author: selene.routley@dlr.de

Received 4 May 2020; revised 14 August 2020; accepted 8 September 2020; posted 8 September 2020 (Doc. ID 396748); published 14 October 2020

Instrumentation design for Fourier transform spectroscopy has until now been hindered by a seemingly fundamental tradeoff between the étendue of the analyzed light source on one hand and the spectral resolution on the other. For example, if a freespace scanning Michelson interferometer is to achieve a spectral resolution of 4 cm^{-1}, it can have a maximum angular field of view of roughly 1° for wavelengths in the neighborhood of $\lambda = 800$ nm, where the general tradeoff for this instrument is that the quotient $\theta_m^2/\Delta k$ of the square of the angular field of view θ_m and the minimum resolvable wavenumber difference Δk is a constant. This paper demonstrates a method to increase the angular field of view allowable for a given resolution by a full order of magnitude, and thus to increase the étendue and, with it, the potential power gathered from an extended source and potential measurement signal-to-noise ratio, by two orders of magnitude relative to the performance of a freespace Michelson interferometer. Generalizing this example, we argue that there may be no fundamental thermodynamic grounds for the tradeoff and that a scanning Fourier transform spectrometer can accept an arbitrarily high étendue field and still, in theory, achieve an arbitrarily narrow spectral resolution.

https://doi.org/10.1364/JOSAA.396748

1. INTRODUCTION

Many applications of spectroscopy deal with point sources and thus light sources of zero entropy, which can be collimated into a lone plane wave beam with unique direction. The classic example here is that of stellar spectroscopy, where the angular subtense of almost all sources is utterly negligible for the purposes of this paper, and indeed the special technique of (long baseline) stellar interferometry [1] is needed to tell most sources from a theoretical point source.

However, the authors' application seeks to average light from as broad a source as possible, so as to average inhomogeneous samples such as grain and soil for compositional analysis. Traditionally, inhomogeneity in spectroscopic compositional analysis is dealt with through wet chemistry and other awkward and work-intensive homogenizing processes, and the authors' application seeks to eliminate these steps so as to bring precision compositional analysis out of the realm of specialized laboratories and into the workplace in agriculture, medicine, and many other everyday industries and also to open the technique to any intelligent non-specialist. A good overview for the kinds of measurement application the authors seek to facilitate can be found in Refs. [2,3].

The increase in allowable source breadth not only brings high resolution spectroscopy to inhomogeneous samples, but can also increase the gathered light power/signal-to-noise ratio for the analysis of certain extended homogeneous sources. The truth of this statement clearly depends on where exactly the instrument's signal-to-noise ratio is limited, but it holds, for example, in the compositional analysis of either the Earth's or another heavenly body's atmosphere. An atmosphere subtends the whole field of view of almost any imaginable spectroscope (up to the half-sphere), so the gathered power and signal-to-noise ratio is ultimately limited by the spectroscope's angular field of view.

Given these motivations, this paper communicates what the authors believe is a wholly new technique to allow a considerable increase in the angular field of view of a scanning Fourier transform (FT) spectroscope. This technique is the subject of a provisional Australian patent [4]. To make this communication, Section 2 first describes how the angular field of view limit arises in a scanning freespace FT–Michelson or Mach–Zehnder interferometric spectroscope, and thus introduces the concepts of (1) the off-axis path difference error (OxPaDE), which is the difference between the phase difference measured

by the interferometer for a perfectly on-axis plane wave and that of an off-axis plane wave, and (2) the Taylor coefficients that define the OxPaDE as functions of the deviation of the off-axis wave's direction from the interferometer's optical axis. It is the OxPaDE that ultimately sets the interferometer's allowable angular field of view, and so our new technique seeks to cancel or minimize the OxPaDE over as wide an angular field of view as possible. Conceptually, the simplest idea is mathematically described by the conditions for cancellation of the quadratic OxPaDE Taylor coefficients; in practical systems, a condition of slightly off-quadratic cancellation yields a minimization over a wider interval as defined, for example, by a minimax criterion, or by a designer's numerical analysis for a specific application. In Section 3, we meet the tilting glass Michelson interferometer [5,6], a device with an OxPaDE function radically different from that of the conventional freespace Michelson FTIR spectrometer. This is a method alternative to the more common idea, such as used in the wishbone interferometer [7] or naïve linear scanning of a corner-cube retroreflector, for the accurate upholding of a Michelson interferometer's second-of-arc accurate alignment while the instrument scans. Next, Section 4 describes our new technique itself in light of the aforesaid concepts. Section 6 briefly studies our idea from a Hamiltonian/thermodynamic-theoretic standpoint to conjecture that the usual tradeoff that arises in a scanning FT interferometer between allowable étendue and spectral resolution is not a fundamental thermodynamic notion, but rather is particularly the interferometer's practical details, and therefore, the ultimate limit in this tradeoff is simply the practical difficulty of confining a widely divergent system of plane waves, as present in a high étendue field, in an instrument that must be kept as small as possible to limit the degrading effects of vibration.

2. ANGULAR FIELD OF VIEW LIMITATION

We begin by taking heed that any freespace spectrometer, whether a scanning FT interferometer or a grating-grounded instrument, ultimately does not measure wavelength/wavenumber but rather a component $k_z = \langle \mathbf{k}, \hat{\mathbf{z}} \rangle$ of the spatial wavevector $\mathbf{k}$ in the optical axis direction $\hat{\mathbf{z}}$. This difference is schematically shown for a scanning Michelson interferometer in Fig. 1, and shows that the fundamental measurand is $k \cos\theta$, but Fig. 1 also holds for a grating spectrometer as follows. The Bragg equation is an expression involving $k_x = \langle \mathbf{k}, \hat{\boldsymbol{x}} \rangle$, where $\hat{\boldsymbol{x}}$ is the transverse direction normal to both the grating's face and to its rills. Off-axis waves whose directions deviate in the $\hat{\boldsymbol{x}}$ direction are mechanically culled by the resolution defining slit, so that each x-bin of the grating's analyzed set of fields comprises waves such that $k_x = k \cos\theta \sin\phi_0$, where ϕ_0 is the constant angle between the incoming optical axis and the grating's face in the nominal plane of diffraction. The interferometer/grating will infer the same measurement result k_{meas} for any wave with a combination of k and θ, with $k \cos\theta = k_0$ for some constant k_0, and therefore, the "error factor"

$$\Delta k = k(1 - \cos\theta) \approx \frac{k}{2}\theta^2 \tag{1}$$

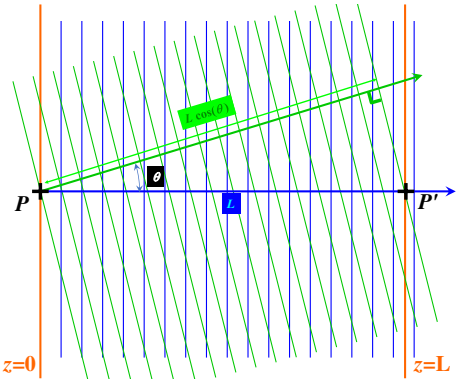

Fig. 1. Freespace interferometer's fundamental measurand.

defines the uncertainty in the inferred wavenumber that arises when we allow the interferometer/grating to measure waves that deviate up to an angle θ from the optical axis. Following this reasoning further, if we set $k/(2\pi) = 1/(0.8 \times 10^{-4}\ \text{cm}) = 12500\ \text{cm}^{-1}$ and we wish to achieve $\Delta k/(2\pi) = 2\ \text{cm}^{-1}$ so that $\pm\Delta k$ spans a $4\ \text{cm}^{-1}$ interval, then we intuitively foresee that our maximum allowable θ is on the order of, given Eq. (1), $\theta \approx \sqrt{2\Delta k/k} \approx 0.0179$ rad $\approx 1°$, and we foresee on the order of 1° allowable angular field of view. This equation agrees with a common design guideline [8] of $\sqrt{\Delta k/k_{\text{max}}}$ modulo a factor of $\sqrt{2}$ (here k_{max} is the maximum wavenumber in the analyzed light), and Fig. 1 is by far the easiest way to intuitively understand such guidelines.

This idea can be analyzed more rigorously in the case of the scanning interferometer as follows. If the optical path between two parallel planes is L for a wave propagating orthogonally to the planes, then the optical path between them for a wave making an angle θ with the plane normal is $L \cos\theta$. The OxPaDE $\Delta\Pi$ for the freespace Michelson interferometer when the nominal path difference is L is therefore

$$\Delta\Pi = L - L\cos\theta \approx \frac{L}{2}\theta^2, \tag{2}$$

where the OxPaDE is the difference between the interferometer's path difference that prevails for an on-axis wave and that that prevails for the off-axis wave in question. The OxPaDE is a function of the off-axis beam direction. Therefore, if an interferometer's input comprises an extended source that, when collimated, gives rise to a uniformly lit cone of plane waves spread over a cone half-angle of θ, and if the interferometer's path difference is L for an on-axis wave, then the interferometer's normalized power output as a function of path difference L is

$$P = 1 - \frac{\int_0^\theta 2\pi \sin\varphi \cos(kL\cos\varphi)\, \mathrm{d}\varphi}{\int_0^\theta 2\pi \sin\varphi \mathrm{d}\varphi}$$

$$\approx 1 - \cos(kL)\,\mathrm{sinc}\left(kL\,\frac{\theta^2}{4}\right), \tag{3}$$

where here the power is normalized with respect to the total power gathered. The latter is proportional to

$$P_0 \propto \int_0^{\theta} \sin\varphi \mathrm{d}\varphi = 1 - \cos\theta \approx \frac{\theta^2}{2}. \tag{4}$$

Equation (3) says that the visibility of the interference fringes is $\mathrm{sinc}(\frac{kL}{2}(1-\cos\theta))$, whereas the total power is proportional to $1-\cos\theta$. The interference signal is then proportional to $\theta^2\mathrm{sinc}(kL\frac{\theta^2}{4})$ and thus, as θ increases, becomes an oscillatory function of wavelength with deep nulls once $kL\frac{\theta^2}{4}$ is a significant fraction of or greater than π. For sound working of the interferometer, therefore, the path difference can only be such that $2\pi\frac{L}{\lambda}\frac{1}{2}(1-\cos\theta) \approx \frac{\pi}{2}$ or

$$L \lessapprox \frac{\lambda}{\theta^2}. \tag{5}$$

The spectral resolution of the FT scanning Michelson interferometer is given by

$$\frac{\Delta k}{2\pi} = \frac{1}{2L}, \tag{6}$$

the factor 2 arising from the there-and-back passing of the beam through the path difference L inside the interferometer. The factor 2 becomes unity for a scanning Mach–Zehnder interferometer. When we substitute Eq. (6) into Eq. (5) we reproduce the same expressions as we found above by the more "intuitive" reasoning.

It should now be clear that the essential notion defining the interferometer's allowable angular field of view as a function of resolution is the OxPaDE as a function of directional deviation from the interferometer's optical axis. If we can make this deviation very small for a wide range of deviations, then the interferometer's field of view will be greatly increased. In the above, the OxPaDE is an axisymmetric function of the beam deviation, i.e., $\Delta\Pi$ depends only on the magnitude of the angular deviation θ from the optical axis, but we are about to encounter situations where this axis symmetry no longer holds. To express the general dependence of the OxPaDE, we need full co-ordinates for the deviation direction. Naturally, any atlas of charts for the unit celestial sphere $\mathbb{S}^2$, such as 2D spherical coordinates, will work; however, in this paper, the two Cartesian direction cosines γ_x, γ_y for the two directions transverse to the system optical axis are used. In general the magnitude of the angular deviation is $\sin\theta = \sqrt{\gamma_x^2+\gamma_y^2}$, but for the angles considered in this paper, we shall assume $\sin\theta \approx \theta$ and that the geometry of the celestial sphere of directions is approximately Euclidean over this restricted range. Therefore, the OxPaDE of Eq. (2) in this notation is

$$\Delta\Pi(\gamma_x, \gamma_y) = \frac{L}{2}\left(\gamma_x^2+\gamma_y^2\right). \tag{7}$$

3. TILTING GLASS INTERFEROMETERS

We now meet a non-axisymmetric OxPaDE, that of the tilting glass Michelson interferometer of Refs. [5,6]. This device is schematically shown in Fig. 2 and comprises a Michelson interferometer with a refractive optical flat straddling both beams and that is rotated symmetrically about the zero pathlength difference point (as suggested by the dashed outlines in Fig. 2) to scan the path difference. The zero pathlength difference point is when the refractor is vertical, and straddling the interferometer arms symmetrically. If a plane wave is incident, with incidence angle θ, on a parallel faced refractive slab of normal thickness t, then the wave is output from the slab with the same propagation direction as it had before input to the slab, and the optical path traveled by the wave is increased by the slab's presence. The optical path difference resulting from the slab's presence (i.e., the optical path of the wave at any phasefront beyond the output less what the optical path value would be were the slab absent) is

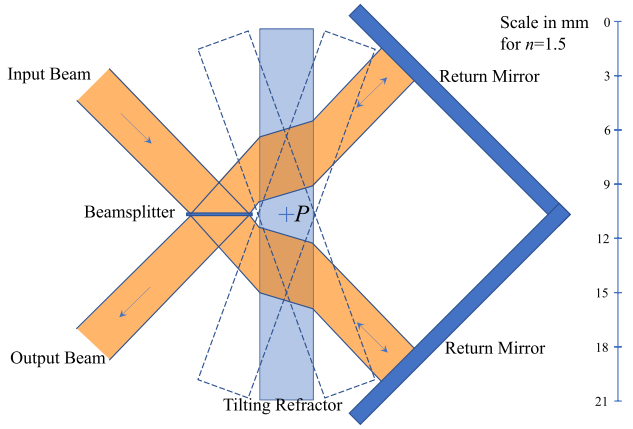

Fig. 2. Basic tilting glass arrangement of Ref. [5].

$$\Phi_0(\theta, t, n) = \left(\sqrt{n^2-\sin^2\theta} - \cos\theta\right) t, \tag{8}$$

where n is the slab's refractive index. In keeping with the fundamental relationship between path difference and ray sideways shear as described in Ref. [9], Section 5.1, the sideways translation of a beam by the slab's presence is given by $\partial\Phi/\partial\theta$:

$$\Delta_0(\theta, t, n) = \frac{\partial\Phi_0}{\partial\theta} = \sin\theta\left(1 - \frac{\cos\theta}{\sqrt{n^2-\sin^2\theta}}\right) t. \tag{9}$$

We first consider the path difference if a ray is input perfectly on-axis in a perfectly aligned Michelson interferometer with tilting glass, as in Fig. 2. In this case, the split copies of the ray propagate through the slab and are reflected from the interferometer's mirrors precisely along the paths along which they are incident to the mirrors, and the two copies retrace their input paths whence they came perfectly back the precise point where the original ray was input to the instrument; there they interfere at the beam splitter.

If the glass is vertical in Fig. 2, both interferometer beams cross the slab at 45° incidence angle. If the slab is tilted at an angle from the vertical, the beam in one Michelson arm has a greater pathlength than the other, and, from Eq. (8), the total interferometer path difference is

$$\begin{aligned}\Phi_1(\theta, t, n) &= \Phi_0\left(\theta+\frac{\pi}{4}, t, n\right) - \Phi_0\left(\frac{\pi}{4}-\theta, t, n\right)\\ &= \sqrt{2}\left(2\sin\theta + \sqrt{2n^2-1-\sin(2\theta)}\right.\\ &\quad\left. - \sqrt{2n^2-1+\sin(2\theta)}\right)t.\end{aligned} \tag{10}$$

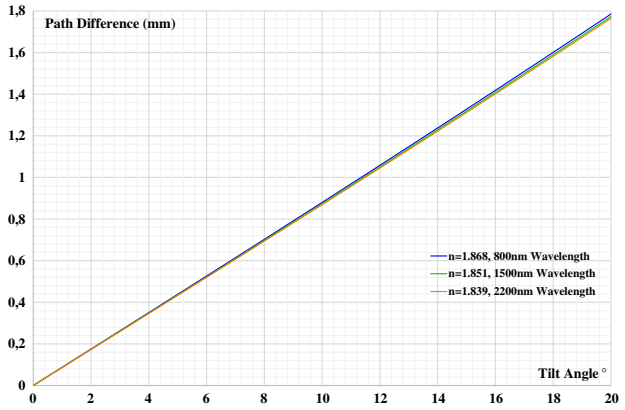

Fig. 3. Tilting glass path difference as function of θ for N-LASF31A glass slab at $\lambda = 800$ nm, 1500 nm, 2200 nm.

This function is plotted in Fig. 3 and is shown to be remarkably linear in Fig. 4.

It should be noted that Dybwad's [5,6] original scheme did not needfully have a 45° beam splitter (indeed a 30° one was used). In this case, the mirrors are not orthogonal; indeed the angle between them is 2α, where α is the angle of incidence of the input beam on the beam splitter. Above, we have assumed $\alpha = \pi/4$ for simplicity. This restriction is relaxed in the following.

To analyze the étendue processing capabilities of a system, one needs to analyze the effect of an off-axis ray. Equation (10) must therefore be modified to account for the fact of different incident and reflected paths in the interferometer. This task is more readily done if Eq. (8) is written in geometric terms only (i.e., free of coordinates):

$$\Phi_0(\boldsymbol{\gamma}, \boldsymbol{\eta}, t, n) = \left(\sqrt{n^2 - 1 + \frac{\langle \boldsymbol{\gamma}, \boldsymbol{\eta}\rangle\langle \boldsymbol{\gamma}, \boldsymbol{\eta}\rangle}{\langle \boldsymbol{\gamma}, \boldsymbol{\gamma}\rangle\langle \boldsymbol{\eta}, \boldsymbol{\eta}\rangle}} - \frac{|\langle \boldsymbol{\gamma}, \boldsymbol{\eta}\rangle|}{\sqrt{\langle \boldsymbol{\gamma}, \boldsymbol{\gamma}\rangle\langle \boldsymbol{\eta}, \boldsymbol{\eta}\rangle}}\right) t, \tag{11}$$

where $\boldsymbol{\gamma}$ is a vector along the ray and $\boldsymbol{\eta}$ a vector showing the normal direction to the slab's surface. Since both arms in the interferometer are nominally identical in the absence of the slab, we analyze them both separately and, without loss of generalness, choose the z axis to be the system's optic axis.

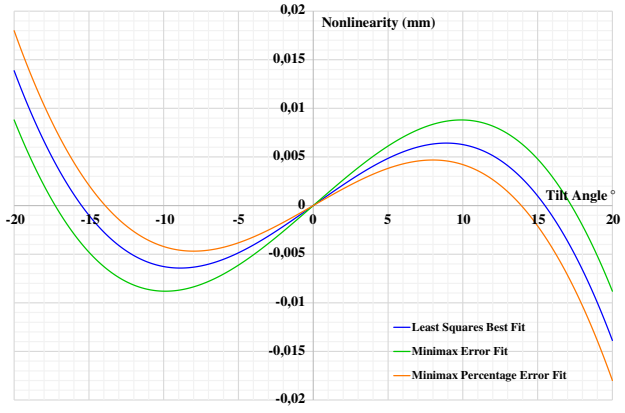

Fig. 4. Tilting glass Michelson interferometer path difference nonlinearity as a function of tilt angle, for $n = 1.851$ and $t = 3$ mm.

Therefore, we can describe an off-axis ray by its transverse direction cosines γ_x, γ_y so that the incident ray is described by the vector

$$\boldsymbol{\gamma}_i = \left(\gamma_x, \gamma_y, \sqrt{1 - {\gamma_x}^2 - {\gamma_y}^2}\right), \tag{12}$$

and the ray reflected from the mirror is then

$$\boldsymbol{\gamma}_r = \left(\gamma_x, \gamma_y, -\sqrt{1 - {\gamma_x}^2 - {\gamma_y}^2}\right). \tag{13}$$

For a slab tilted in the plane of the page in Fig. 2, which can be assumed to be the (x, z) plane, the slab normal vector is $\boldsymbol{\eta} = (\sin\theta, 0, \cos\theta)$, so that the total delay of the round ray trip, on application of Eq. (11), is

$$\begin{aligned}\Phi(\gamma_x, \gamma_y, \theta, t, n) &= \left(\sqrt{n^2 - 1 + \left(\sqrt{1 - {\gamma_x}^2 - {\gamma_y}^2}\cos\theta + \gamma_x \sin\theta\right)^2}\right. \\ &\quad - 2\sqrt{1 - {\gamma_x}^2 - {\gamma_y}^2}\cos\theta \\ &\quad \left. + \sqrt{n^2 - 1 + \left(\sqrt{1 - {\gamma_x}^2 - {\gamma_y}^2}\cos\theta - \gamma_x \sin\theta\right)^2}\right) t,\end{aligned} \tag{14}$$

so that the full expression for the path difference wrought by the interferometer in Fig. 2 when the slab is tilted at an angle θ from the vertical in Fig. 2 is

$$\begin{aligned}\Pi(\gamma_x, \gamma_y, \theta, t, n) &= \Phi\left(\gamma_x, \gamma_y, \theta + \frac{\pi}{4}, t, n\right) \\ &\quad - \Phi\left(\gamma_x, \gamma_y, \theta - \frac{\pi}{4}, t, n\right).\end{aligned} \tag{15}$$

The above reasoning repeated for an interferometer whose slab rotates in the (y, z) shows that the result is the same as Eq. (15), but with γ_x and γ_y swapped, i.e., the path difference is $\Pi(\gamma_y, \gamma_x, \theta, t, n)$.

The sideways shear of the beam is, by the relationships of Ref. [9], Section 5.1, given by the transverse vector whose components are

$$\Delta_x = \frac{\partial \Pi(\gamma_x, \gamma_y, \theta, t, n)}{\partial \gamma_x}; \quad \Delta_y = \frac{\partial \Pi(\gamma_x, \gamma_y, \theta, t, n)}{\partial \gamma_y}. \tag{16}$$

To second order, Eq. (15) evaluates to

$$\Pi(\gamma_x, \gamma_y, \theta, t, n) \approx \Phi_1(\theta, t, n) + \xi_x {\gamma_x}^2 + \xi_y {\gamma_y}^2, \tag{17}$$

with transverse beam shear

$$\Delta \approx 2\sqrt{{\xi_x}^2 {\gamma_x}^2 + {\xi_y}^2 {\gamma_y}^2}, \tag{18}$$

and the defining coefficients are

$$\xi_x = -\sqrt{2}\sin\theta + \frac{\left(8n^2-4\right)\sin 2\theta - \cos(4\theta) + 3}{2\sqrt{2}\sqrt{2n^2+\sin(2\theta)-1}^3} + \frac{\left(8n^2-4\right)\sin 2\theta + \cos(4\theta) - 3}{2\sqrt{2}\sqrt{2n^2-\sin(2\theta)-1}^3}$$

$$\xi_y = -\sqrt{2}\sin\theta + \frac{\sin 2\theta + 1}{\sqrt{2n^2+\sin(2\theta)-1}} + \frac{\sin 2\theta - 1}{\sqrt{2}\sqrt{2n^2-\sin(2\theta)-1}}, \tag{19}$$

which are swapped when the tilting glass rotation plane is changed from the $(x,\ z)$ plane to the $(y,\ z)$ plane.

Naturally, all these equations are readily broadened to cope with the case where the two Michelson beams intersect at angles other than a right angle by simple application of the above reasoning. In the following, α is the nominal angle of incidence of the input beam on the beam splitter; this angle has hitherto been assumed to be $\pi/4$, but, as noted above, there is no requirement in either the Dybwad [5,6] tilting glass interferometer or in our new OxPaDE quadratic coefficient cancellation/minimization scheme below for this angle to be 45°.

The double-pass transmission through the tilting glass that happens in the Michelson interferometer makes Eq. (14) an even function of γ_x and of γ_y, so that the largest error terms in Eq. (14) are second order. If there is only a single pass of the glass, then Eq. (14) would not have its even symmetry in γ_x, and a linear, much larger term would result, thus destroying the fundamental mechanism of the quadratic OxPaDE cancellation scheme. It is therefore foreseen that the scheme would be realized mostly by a Michelson or other double-pass interferometer.

One can also change the refractive index of the slab, and this variation gives rise to the dependence shown in Fig. 5.

For high refractive indices, the OxPaDE coefficients of Eq. (19) can be considerably smaller than their values for a freespace Michelson or Mach–Zehnder interferometer. For $n = 2.0951$ and $|\theta| \le 20\pi/180$ (i.e., $|\theta| \le 20°$), the values as a function of tilt angle are equal in magnitude, as shown in Fig. 5. Already, without the quadratic OxPaDE cancellation

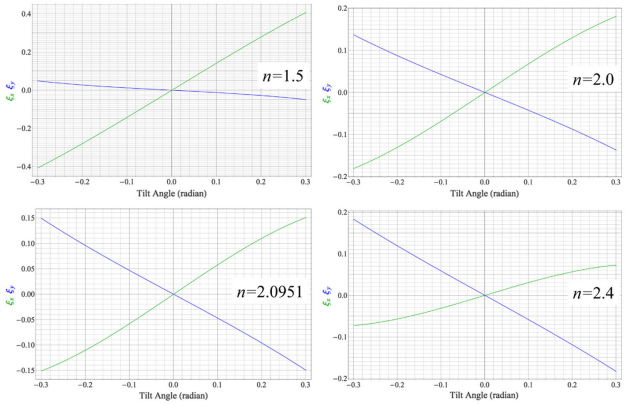

Fig. 5. Off-axis pathlength error coefficients ξ_x (green) and ξ_y (blue) as functions of the glass angular deviation from the zero pathlength point for the simple tilting glass Michelson interferometer for different slab refractive indices. Note the swap in magnitudes of the gradients as the index increases.

scheme, these values are considerably less than the corresponding values ($\xi_x = \xi_y = 1/2$) for a simple freespace Michelson interferometer. If the maximum tilt were restricted to 8°, then we would have $\xi_x = -\xi_y = 0.08$ and would allow a Jacquinot stop of approximately $\sqrt{1/(2\times 0.08)}$ times the diameter that a freespace Michelson interferometer would allow for the same signal-to-noise ratio loss through the fringe fading phenomenon discussed in Section 2. This represents a sixfold ($= 1/(2\times 0.08)$) increase in the instrument's throughput and thus potentially signal-to-noise ratio for no loss of spectral resolution.

4. QUADRATIC OFF-AXIS PATH DIFFERENCE ERROR CANCELLATION

Given the foregoing analysis, we make the following crucial observations:

- the coefficients ξ_x, ξ_y as functions of the tilt angle θ as defined are of opposite sign;
- for low refractive index, $|\xi_x| > |\xi_y|$, and for high refractive index, this order is swapped ($|\xi_x| < |\xi_y|$), and there exists a critical effective refractive index of approximately 2.183 at which the two functions are negatives of one another ($\xi_x \approx -\xi_y$) to a very good approximation, as in the bottom left plot of Fig. 8;
- the functional dependence of ξ_x, ξ_y on the tilt angle θ is swapped if one changes the rotation plane of the tilting glass to the orthogonal rotation plane, e.g., with the optical axis assigned to the z axis, if the rotation plane is changed from the $(x,\ z)$ to the $(y,\ z)$ plane.

Therefore, if the Michelson interferometer's path difference is realized by two or more tilting glasses for each arm wherein

- the effective index of both glasses is engineered to be approximately 2.183 (or whatever value is appropriate for the error minimization criterion, e.g., 2.16915 if the minimax criterion of Section 7 is used);
- the glasses rotate both through the same angle and of sense (relative to the light beam that passes through them) such that the phase difference contributions by each to the interferometer's path difference add to enhance one another;
- the rotation planes of glasses contributing half the path difference are orthogonal to the rotation planes of the contributing other half, then the quadratic OxPaDE coefficients of the whole interferometer cancel to almost zero, and the instrument will impart no OxPaDE to second order. Practically, this means that Jacquinot stops subtending many times the angle allowable in a freespace interferometer can be used with little or no loss of spectral resolution. The throughput through the system, thus potentially signal-to-noise ratio, can therefore be increased by at least one and possibly two orders of magnitude.

To illustrate the above further, we present two conceptual realizations. The first, and conceptually simplest, is shown in Fig. 6. The system comprises a beam splitter and folding mirrors to realize a Michelson interferometer with two parallel arms defined by the two parallel plane mirrors. The tilting glasses each comprise two identical sections, one section for each arm, and the sections are at right angles to one another. Therefore, the system in Fig. 6 would be precisely equivalent to the Dybwad

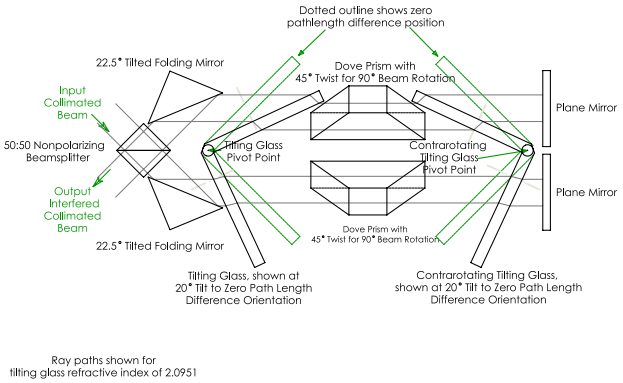

Fig. 6. Use of two Dove prisms for 90° beam rotation between tilted glasses contra-rotating symmetrically about the zero-point position.

lone tilting glass scheme in Fig. 2 if one of the two section tilting glasses and the Dove prisms were absent; in this case, the zero pathlength difference point would be where the remaining tilting glass were aligned symmetrically, as shown by the dotted outline, relative to the two Michelson arms. When the Dove prisms and second tilting glass are introduced, and when both tilting glasses contrarotate so that the angle made between each glass and the beam in either of the arms is always precisely the same (i.e., the glasses contrarotate the same amount about the zero pathlength difference configuration shown by the dotted outlines), then the total there-and-back phase difference is given by the following modification of Eq. (17):

$$\tilde{\Pi}\left(\gamma_x,\ \gamma_y, \theta,\ t,\ n\right) \approx 2\Phi_1(\theta,\ t,\ n) + \left(\xi_x + \xi_y\right)\left({\gamma_x}^2 + {\gamma_y}^2\right), \tag{20}$$

because the Dove prisms, each parallel to the arm and rotated azimuthally about their central axes through a 45° angle, rotate the beams about their centers through 90°. Therefore, the roles of ξ_x and ξ_y are swapped for the second tilting glass, and the second-order coefficients of γ_x^2 and γ_y^2 are identical in Eq. (20) and both equal to $\gamma_x + \gamma_y$, with γ_x, γ_y both defined by Eq. (19). Therefore, when we tune the glass refractive index as described above to realize $\xi_x = -\xi_y$, the system in Fig. 6 realizes the scheme described above and has vanishing quadratic OxPaDE coefficients.

The Dove prism scheme may be the easiest conceptually to understand, but it is probably not the most practical. High étendue collimated fields are still highly divergent, since they comprise a classical incoherent mixture of near to plane waves spread over a spectrum of directions. For example, as will become clearer in the following, the authors believe that when system tolerances and imperfections are considered, a practically attainable enhancement available from the quadratic OxPaDE cancellation idea is the increasing of the angular field of view of a 4 cm^{-1} scanning FT–Michelson interferometer from the 1° cone half-angle cited in Section 2 to a 7° cone half-angle. A field with a 14° spread of angles diverges quickly, and the arm lengths must be kept as short as possible if the interferometer's overall dimensions are to be kept reasonably small. Not only is a small instrument convenient for portable testing applications, but an important design doctrine in FT interferometry is to keep dimensions as small as possible and structural frames as stiff as possible to manage the effect of vibration on the instrument. These guidelines keep vibration eigenfrequencies outside the realm of likely excitation through routine, portable instrument mechanical shock. A sound acoustic design is essential to an instrument's success if it is used in out-of-laboratory, portable applications.

5. PRACTICAL SYSTEM CONSIDERATIONS

Therefore, the authors propose the architecture shown in Fig. 7 as a more practical proposal. Figure 8 shows a plan view of the system with the major parts labeled as a more schematic diagram. The system dimensions in the plan are approximately 120 mm × 120 mm for a 7 mm wide collimated beam at its Fourier plane/pupil. As shown in Fig. 9, the system pupils are always designed to lie on the return mirrors at the end of each Michelson arm, for maximum high étendue beam containment/minimum system size. This system comprises the single tilting glass of the system in Fig. 2, but with two further identical tilting glasses, one placed in each Michelson arm, rotating about axes orthogonal to both the rotation axis of the main tilting glass and the optic axis of each respective Michelson arm. Each of the further two glasses rotates so as to add to the phase imparted to the respective arm by the main tilting glass and always to make the same angle with the optic axis of the respective arm as the main tilting glass. As schematically shown in Figs. 7 and 8, this is probably most effectively done by affixing the angular position sensing digital shaft encoders and electromagnetic rotational actuators to each of the three rotation axes and the use of a computer control system to continuously sense the position of each shaft and drive the rotational actuators so as to impart the path difference scan needed for FT spectroscopy while upholding the relationships between the shaft angles needed to ensure that $\xi_x \approx -\xi_y$ at all times.

We shall now use the equations and analysis in Section 7, Eq. (32), to analyze the performance of the scheme in Figs. 7–9 in the face of real-life imperfections such as tracking error and material dispersion. The former problem is where the actuators fail to uphold the relationships between the angular positions of the tilting glasses necessary for $\xi_x \approx -\xi_y$ perfectly, and tracking is accurate only to within a nonzero angular tracking error. The latter is the inevitable deviation of the refractive index of the tilting glasses from the target value needed to achieve the

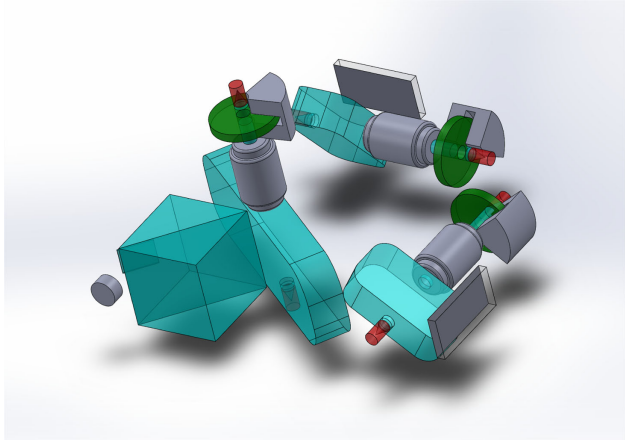

Fig. 7. Proposed practical quadratic OxPaDE cancellation scheme.

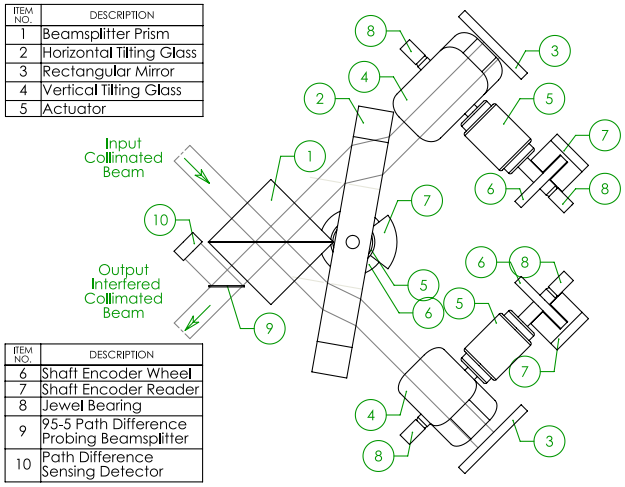

Fig. 8. Plan view of the essential components of a practical quadratic OxPaDE cancellation scheme.

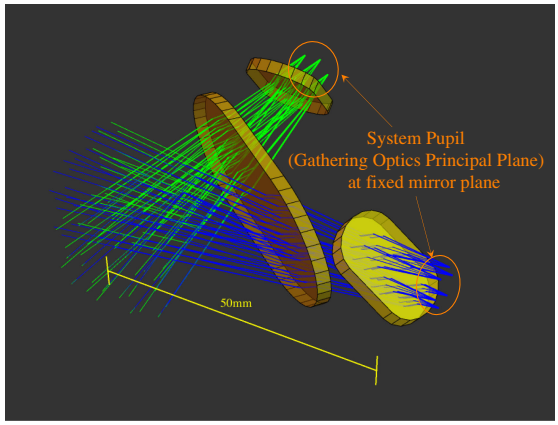

Fig. 9. System pupils placed on return mirrors.

quadratic OxPaDE cancellation condition $\xi_x \approx -\xi_y$, since a FT spectrometer must inevitably process a broad range of wavelengths, and the glasses needed to realize the high refractive indices necessary to achieve this condition are needfully quite dispersive over these ranges. For a concrete example, we consider the scheme in Fig. 7 processing a high étendue light field defined by collimated beams of 7 mm diameter whose directions are uniformly distributed in a direction cone of half-vertex angle 7° (123 mrad). The tilting glasses are all 2.5 mm thick, their angular scan range is ±8°, and they are assumed to have an index of 2.16915, which is the value defined by the minimax criterion in Section 7, especially Eq. (26), for a scheme with a tilt range of ±8°. Figures 10 and 11 plot the OxPaDE in nanometers as a function of (γ_x, γ_y), as the latter two individually range over the intervals ±8°. Both these figures hold for an angular deviation of 5° from the zero pathlength difference condition; as shown in Fig. 12, this position is the position of minimize maximum OxPaDe for the minimax tuning of the glass refractive index for the ±8° range. In the perfect case, the maximum minimax error in the ±8° range of (γ_x, γ_y) is about 20 nm. Figure 11 shows the same plot when the two secondary tilting glasses are offset by 0.1°, with the same sign of error in both cases, from their perfect angular position of 5° from the zero pathlength difference position that would match the 5° position of the main tilting glass. In this case, we see that the rotational symmetry in Fig. 10 has been broken, and the maximum minimax error in the ±8° range of (γ_x, γ_y) has risen to about 50 nm. The case where one of the secondary tilting glasses leads the main glass by

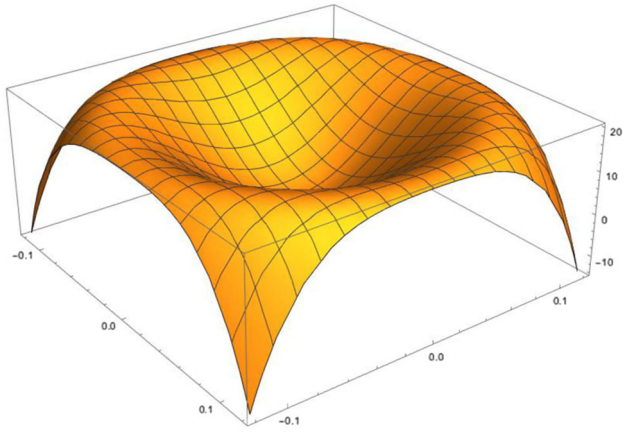

Fig. 10. OxPaDE as a function of (γ_x, γ_y) for perfect tilt glass tracking; vertical scale ranges from −10 nm to +20 nm.

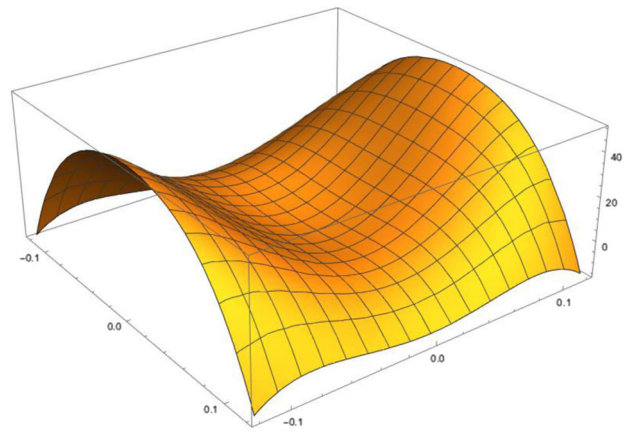

Fig. 11. OxPaDE as a function of (γ_x, γ_y) for tilt glass tracking with a 0.1° (1.75 mrad) tracking error; vertical scale ranges from −10 nm to +50 nm.

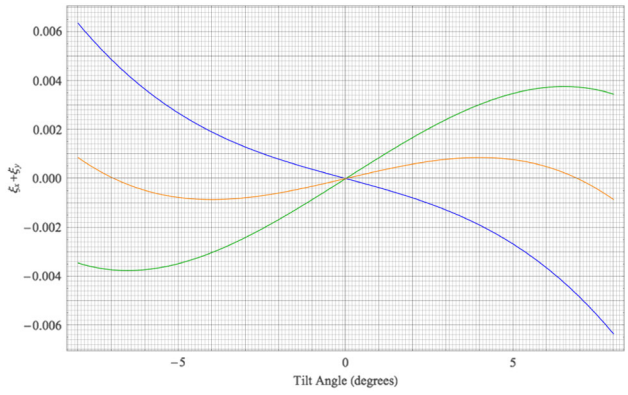

Fig. 12. Plots of $\xi_x + \xi_y$ for $\lambda = 800$ nm (blue), $\lambda = 1200$ nm (orange), and $\lambda = 2200$ nm (green).

Table 1. Indices of Glasses Used in the Effective Index Scheme of Section 7

	$\lambda = 800$ nm	$\lambda = 1200$ nm	$\lambda = 2200$ nm
ZnSe	2.526	2.470	2.443
LASF35	1.998	1.982	1.962

0.1° and the other lags by 0.1° was also simulated and found to cause a much smaller increase in maximum minimax error.

The other practical effect we must be aware of is dispersion, as there would seem to be no way to counteract dispersion effects in zero optical power optics (i.e., optical flats). However, the effects of dispersion are not great over the infrared range; the effects would be severer at visible wavelengths nearer to the relevant transition frequencies of glasses. We examine the effective index method in Section 7 over a wide wavelength range. The refractive indices for ZnSe and LASF35 in Table 1 will be used.

If we implement the scheme in Section 7, Eq. (32), for a ±8° tilting range optimized for $\lambda = 1200$ nm, we get $r = 0.438136$. The effectiveness of the scheme can be assessed by plotting $\xi_x + \xi_y$ as a function of θ over the tilt range for different wavelengths within the working wavelength range as in Fig. 12. This figure shows that the error cancellation is still extremely effective over the whole wavelength range. Recall that the simple freespace Michelson interferometer has $\xi_x = \xi_y = 1/2$. At the optimal wavelength of $\lambda = 1200$ nm, the maximum minimax $\xi_x + \xi_y$ is about 8×10^{-4}, meaning that the angular field of view (in degrees) can be increased relative to the freespace Michelson by a factor of $\sqrt{0.5/0.0008} \approx 25$. The worst case in Fig. 12 is $\lambda = 2200$ nm, implying that the angular field of view increase available is a factor of $\sqrt{0.5/0.0006} \approx 9$. For our present studied scheme, where the target angular field of view is ±7°, the onset of vignetting will still limit the system's performance before the limits implied by Fig. 12 become dominant.

Thus, we have shown that the scheme is extremely promising, even in the face of nonideal effects such as imperfect tracking and material dispersion. The use of 14-bit shaft encoders together with direct drive angular position actuators (to eliminate all drive backlash) and the appropriate digital loop control system should easily allow to achieve the required angular relationships among the three shafts to within 0.1°. An increase in available angular field of view for a 4 cm^{-1} scanning Michelson–FT interferometer spectroscope from ±1° up to ±7° would seem quite feasible.

Last, one highly salient practical advantage of tilting glass FT spectrometers as opposed to those that linearly scan their pathlength differences is their natural resilience to vibration, one of the main motivations for Dybwad in creating his 1987 tilting glass scheme and an advantage that is heavily emphasized in the patent [5,6]. Inertial forces arising in the instrument when it is mechanically disturbed act at the center of mass of tilting glasses, whose center is easily arranged through balanced design to be the center of rotation of the tilting glasses. Therefore, inertial forces directly impart minimal disturbing torque to the glasses. Likewise, if the tilting glasses are mechanically coupled to the rest of the instrument through small, rotationally symmetric bearings such as jewel bearings, forces transmitted to them from the rest of the instrument also act through the rotation axis and thus impart minimal disturbing torque.

It is true that acoustic waves acting out of phase on the Michelson arms can impart a spurious linear scan to the instrument. However, for a device as small as proposed in Section 5, this linear pathlength difference scan is readily constrained to lie within to the order of 1 μm with sound acoustic isolation and structural engineering. Acting over a pathlength difference $L = 1$ μm in Eq. (7), the freespace OxPaDe arising from a vibration of such magnitude is negligible, and as long as a closed-loop pathlength difference sensing mechanism (e.g., fringe counting interferometry done on a "pilot" or "tracking" wavelength) correctly registers the pathlength change arising from the vibration, its effect can be fully corrected for in data processing before the FT spectrum is computed. A future paper will address this pathlength difference sensing problem.

6. CONCLUSION: THERMODYNAMIC/HAMILTONIAN/SYMPLECTIC DYNAMICS CONSIDERATIONS

This paper has demonstrated a new titling glass Michelson interferometer for FT spectroscopy that greatly relaxes the angular field of view constraints that have hitherto hindered the ability of FT spectroscopy to process high étendue light, equivalently, light from spatially broad optical sources while upholding high spectral resolution. The interferometer achieves this through an OxPaDE cancellation scheme, physically realized by two components of the phase difference scanning mechanism that mutually enhance their total path difference but that have OxPaDE functions that cancel one another out.

Although the focus and motivation of this paper have been overwhelmingly practical—the creation of highly miniaturized interferometers that can process extremely high étendue fields/broad optical sources without loss of spectral resolution—the theoretical implications of the ability to cancel the OxPaDE in the way we have shown above is truly tantalizing. One at first intuitively expects that there might be a fundamental theoretical tradeoff between the étendue of the field one can spectroscopically analyze and the physical size of the interferometer needed to reach a given spectral resolution. Equation (1) and the reasoning in Section 2 vividly intuitively suggest this tradeoff: a required spectral resolution implies an angular field of view limit. If we think of (the square root of) étendue of a collimated field intuitively as an angular spread of the classically mixed constituent collimated fields times the beam diameter, and given the conservation principle for étendue, then we must magnify the beam diameter with passive optics to shrink the angular spread in inverse proportion to the beam diameter so as to fit the resultant angular spread inside the interferometer's angular field of view that is allowable for our required spectral resolution. But our OxPaDE cancellation scheme shows that the severity of the constraints imposed by this at first seemingly fundamental tradeoff can be hugely slackened. The question now arises as to what, if any, is the fundamental beamwidth/size limit for FT interferometry that may be imposed by the need to analyze high étendue fields. The dramatic cancellation of the OxPaDE we have demonstrated suggests that there may not be

any such fundamental tradeoff. Indeed, in our 4 cm^{-1} resolution spectroscopy example, the angular field of view requirement was relaxed so much that the size constraint arises mainly from the practical consideration of the processing of highly divergent fields without such divergence leading to vignetting and power loss in the parts of the instrument farthest from the system pupils/Fourier planes; this field divergence problem completely overtakes the étendue constraint as a practical design headache!

Ray optics can, as is well known [10–16], be thought of in a Hamiltonian formulation, thus as an evolution of system states in phase space represented by a flow that conserves a symplectic form and heeds Liouville's theorem. These two properties are perhaps more wonted to optical engineers as the conservation of the Helmholtz invariant and the conservation of étendue. It is not widely understood that the latter is a necessary condition, merely a special case of the former, and the symplectic form conservation constraints arising from a Hamiltonian formulation are indeed stronger than simply the conservation of étendue. Beyond ray optics, it is postulated that conservation of étendue holds more generally in all optical systems when étendue is appropriately generalized to the thermodynamic system of property of entropy/Shannon information as simply a manifestation of the second law of thermodynamics. Therefore, study of the OxPaDE cancellation scheme and more fundamental constraints in the spectral processing of high étendue fields by the authors using the tools of Hamiltonian system theory, symplectic geometry, and information theory by the authors is presently intensely underway, and findings resulting from this study will be presented in future academic communications.

7. QUADRATIC OXPADE CANCELLATION: FURTHER ANALYSIS

We now seek to analyze the OxPaDE cancellation scheme above more fully as follows, as well as to explain the minimax error minimization method and effective index method for tuning the refractive index of the tilting glass accurately to the required value, even though no off-the-shelf glass may have this exact index. We begin with the expression

$$\Pi(\gamma_x,\ \gamma_y, \theta, \alpha,\ t,\ n) = \Phi(\gamma_x,\ \gamma_y, \theta+\alpha,\ t,\ n) - \Phi(\gamma_x,\ \gamma_y, \theta-\alpha,\ t,\ n), \tag{21}$$

which generalizes Eq. (15) and which accounts for a generalized Michelson interferometer where the two interfering arms intersect at an angle of 2α, and generalized versions of Eq. (19) are readily shown to be

$$\begin{aligned}
\xi_x &= \cos(\alpha+\theta) - \cos(\alpha-\theta) + \frac{\sin^2(\alpha+\theta) - \cos^2(\alpha+\theta)}{\sqrt{n^2 - \sin^2(\alpha+\theta)}} \\
&\quad + \frac{\cos^2(\alpha-\theta) - \sin^2(\alpha-\theta)}{\sqrt{n^2 - \sin^2(\alpha-\theta)}} + \frac{\sin^2(2\ (\alpha-\theta))}{4\sqrt{n^2 - \sin^2(\alpha-\theta)}^3} - \frac{\sin^2(2\ (\alpha+\theta))}{4\sqrt{n^2 - \sin^2(\alpha+\theta)}^3}, \\
\xi_y &= \cos(\alpha+\theta) - \cos(\alpha-\theta) + \frac{\cos^2(\alpha-\theta)}{\sqrt{n^2 - \sin^2(\alpha-\theta)}} - \frac{\cos^2(\alpha+\theta)}{\sqrt{n^2 - \sin^2(\alpha+\theta)}}.
\end{aligned} \tag{22}$$

Given the constraint ${\gamma_x}^2 + {\gamma_y}^2 \le {\gamma_{\max}}^2$, it is readily shown (by writing $\gamma_x = \gamma_{\max}\cos u,\ \ \gamma_y = \gamma_{\max}\sin u$) that maximum magnitude of the quadratic OxPaDE ${\xi_x}\,{\gamma_x}^2 + {\xi_y}\,{\gamma_y}^2$ is $\gamma_{\max}\max(|\xi_x|, |\xi_y|)$. One can approximate the functions in Eq. (21) for small deviations θ from the zero pathlength difference point; for small angles, the cubic functions of Eq. (23) with Eq. (24) are an excellent approximation for all refractive indices between 1.3 and 3 and for all interferometer beam intersection half-angles α and all tilts θ within the 20° range. This fact about the functions in Eq. (21) can be verified numerically, as well as the fact that for any given α, both $|\xi_x|,\ |\xi_y|$ are monotonic functions of the refractive index in such a way that the maximum $\max(|\xi_x|,\ |\xi_y|)$ is minimized, as a function of the refractive index, where the magnitudes cross over $|\xi_x| = |\xi_y|$, i.e., where $\xi_x = -\xi_y$ or $\xi_x + \xi_y = 0$. Thus, the OxPaDE for a single tilting glass Michelson interferometer is minimized for the same refractive index as is needed to effect quadratic OxPaDE cancellation in Section 4.

In general, as readily seen from Eq. (22), the condition $\xi_x + \xi_y = 0$ depends on θ and so cannot be solved for all tilt angles in a scanning range. However, this function is, to an excellent approximation for tilt angles θ up to 20° (which is the maximum applicable range), extremely well approximated by its third-order Taylor series about $\theta = 0$:

$$\xi_x + \xi_y \approx \Xi_1\,\theta + \Xi_3\,\theta^3, \tag{23}$$

where

$$\begin{aligned}
\Xi_1 &= \frac{\sin(\alpha)}{2\sqrt{n^2 - \sin^2(\alpha)}^5}\left(\cos(\alpha)\left(\cos(4\alpha) + 24\,n^4 + 2\left(5\,n^2 - 3\right)\cos(2\alpha) - 26n^2 + 5\right) - 8\sqrt{n^2 - \sin^2(\alpha)}^5\right), \\
\Xi_3 &= \frac{1}{24}\sin(\alpha)\left(16 + \frac{3\cos(\alpha)\left(\cos(4\alpha) - 64\,n^4 + 4\left(8\,n^2 - 1\right)\cos(2\alpha) - 32\,n^2 + 3\right)}{\sqrt{n^2 - \sin^2(\alpha)}^5}\right. \\
&\quad \left. + \frac{6\cos^5(\alpha)\left(\cos(4\alpha) - 72\,n^4 + \left(38\,n^2 - 4\right)\cos(2\alpha) - 38\,n^2 + 3\right)}{\sqrt{n^2 - \sin^2(\alpha)}^9}\ \frac{\cos^3(\alpha)\left(-11\cos(4\alpha) + 608\,n^4 + \left(44 - 340\,n^2\right)\cos(2\alpha) + 340\,n^2 - 33\right)}{\sqrt{n^2 - \sin^2(\alpha)}^7}\right),
\end{aligned} \tag{24}$$

and so, for a wide range of small angles, the condition $\xi_x + \xi_y = 0$ can be fulfilled by setting $\Xi_1 = 0$, which arises when

$$u^5 - 3\cos\alpha u^4 + \frac{1}{8}(9\cos\alpha + 7\cos(3\alpha))$$

$$u^2 + \frac{3}{2}\cos^3\alpha\sin^2\alpha = 0, \tag{25}$$

where $u^2 = n^2 - \sin^2\alpha$.

Although the equation is quintic in u, there are in fact expressions for exact roots in terms of radicals even though the general expressions for a quintic's roots must involve nonradical (Jacobi elliptic) functions. For $\alpha = \pi/4$, the one real solution to Eq. (25) is $n = 2.183$.

For wider angle ranges, one can choose a refractive index to minimize the maximum value of the cubic $\Xi_1\theta + \Xi_3\theta^3$. This solution can be found in several different ways to show that it arises when Ξ_1, Ξ_3 are of opposite sign (which they are) and

$$\Xi_1 = -\frac{3}{4}\,\Xi_3{\theta_{\max}}^2, \tag{26}$$

where $[-\theta_{\max}, \theta_{\max}]$ is the tilt angle interval wherever the minimax solution is sought. Eq. (26) in general yields the following degree 9 polynomial equation:

$$u^9 + \sigma_8\,u^8 + \sigma_6\,u^6 + \sigma_4\,u^4 + \sigma_2\,u^2 + \sigma_0 = 0, \tag{27}$$

where, as before, $u^2 = n^2 - \sin^2\alpha$, and

$$\sigma_8 = -\frac{12\left(2 - {\theta_{\max}}^2\right)\cos(\alpha)}{8 - {\theta_{\max}}^2},$$

$$\sigma_6 = \frac{\cos(\alpha)\left(\left(14 - 37{\theta_{\max}}^2\right)\cos(2\alpha) + 2 - {\theta_{\max}}^2\right)}{8 - {\theta_{\max}}^2},$$

$$\sigma_4 = \frac{3\cos(\alpha)\left(3{\theta_{\max}}^2\cos(2\alpha) + \left(28{\theta_{\max}}^2 - 2\right)\cos(4\alpha) + 5{\theta_{\max}}^2 + 2\right)}{4\left(8 - {\theta_{\max}}^2\right)},$$

$$\sigma_2 = \frac{15{\theta_{\max}}^2\sin^2(\alpha)\cos^3(\alpha)(21\cos(2\alpha) + 1)}{4\left(8 - {\theta_{\max}}^2\right)},$$

$$\sigma_0 = \frac{105{\theta_{\max}}^2\sin^4(\alpha)\cos^5(\alpha)}{2\left(8 - {\theta_{\max}}^2\right)}. \tag{28}$$

The above reduces to an equation of the form $u^4\,p_5(u) = 0$, where $p_5(u) = 0$ becomes the quintic in Eq. (25) when $\theta_{\max} \to 0$. For a maximum angle of 8° and a right angled Michelson with $\alpha = \pi/4$, the above gives two real solutions, $n = 0.926541$ and $n = 2.16915$. The latter is clearly the minimax solution, and a plot of $\xi_x + \xi_y$ for this value of index is shown in Fig. 9. As betokens the minimax solution in general, the values of the function at the local minimum/local maximum are equal to the functions' values at the ends of the angle range wherein the minimax solution was found.

It is not always practicable to find optical materials with the exact refractive indices for the optimizations of the foregoing section. Therefore, instead, a layered structure can be used for the tilting glasses, with the indices of the layers composing the structure chosen so that the overall effective index is correct. For this scheme to be effective, the indices of the composing layers must be near to the goal refractive index.

For example, suppose we seek a material to solve the annul Taylor coefficient Ξ_1 as in the foregoing section, i.e., we seek to annul $\xi_x + \xi_y$ for small tilt angles. Suppose further that we have only two standard glasses available, say zinc selenide, with a refractive index of $n_1 = 2.47$, and LASF35, with an index of $n_2 = 1.982$, both at $\lambda = 1200$ nm. The tilting glass in question can be made of two layers, such that the ZnSe and LASF35 thicknesses are in the ratios $r : 1 - r$. Since the phase delays through the stacked layers are exactly linearly additive, the Taylor series coefficients in Eq. (23) now become

$$\Xi_{1E} = r\;\Xi_1(n_1,\;\alpha) + (1 - r)\;\Xi_1(n_2,\;\alpha)$$

$$\Xi_{3E} = r\;\Xi_3(n_1,\;\alpha) + (1 - r)\;\Xi_3(n_2,\;\alpha), \tag{29}$$

where $\Xi_i(n_j,\;\alpha)$ is the value of Ξ_i for the index n_j as given by the homogeneous layer Eq. (24) of the jth layer. We now solve the equation $\Xi_1 = 0$ for r. Not all glasses will work with this idea because, of course, the solution to $\Xi_1 = 0$ must have $0 \le r \le 1$ for the solution to be physically realizable. The values of the composing Ξ_1 values are

$$\Xi_1\left(n_1,\;\frac{\pi}{4}\right) = -0.340991; \quad \Xi_1\left(n_2,\;\frac{\pi}{4}\right) = 0.298829, \tag{30}$$

and therefore, a solution is possible with these two glasses with $r = 0.467052$. The minimax equation $\Xi_1 = -\frac{3}{4}\,\Xi_3\,{\theta_{\max}}^2$ can also be solved for r with $\theta_{\max} = 8\,\pi/180$, since

$$\Xi_3\left(n_1,\;\frac{\pi}{4}\right) = -1.11739; \quad \Xi_3\left(n_2,\;\frac{\pi}{4}\right) = -1.38065, \tag{31}$$

with a minimax solution for $r = 0.438136$. The general expression is readily shown to be

$$r = \frac{\Xi_1(n_2,\;\alpha) + \frac{3}{4}{\theta_{\max}}^2\,\Xi_3(n_2,\;\alpha)}{\Xi_1(n_2,\;\alpha) - \Xi_1(n_1,\;\alpha) + \frac{3}{4}\,{\theta_{\max}}^2\,(\Xi_3(n_2,\;\alpha) - \Xi_3(n_2,\;\alpha))}. \tag{32}$$

Funding. Hone Global (Rapid Phenotyping Pty. Ltd.) Research and Development Budget; Deutschen Zentrum für Luft- und Raumfahrt.

Acknowledgment. The authors thank Hone Global (Rapid Phenotyping Pty. Ltd.) for permission to publish this research. S. Routley thanks the Deutsches Zentrum für Luft- und Raumfahrt as a full-time researcher at that institute for Optical Sensor Systems for the opportunity to explore ongoing applications of the technology of mutual benefit to both Hone and the DLR.

Disclosures. SAR: Hone Ag Pty. Ltd. (I, E, P), Deutsches Zentrum für Luft und Raumfahrt (E), JF, AM, WP: Hone Ag Pty. Ltd. (I, E, P).

REFERENCES

1. J. D. Monnier, "Optical interferometry in astronomy," Rep. Prog. Phys. **66**, 789–857 (2003).

2. R. A. V. Rossel and R. Webster, "Predicting soil properties from the Australian soil visible–near infrared spectroscopic database," Eur. J. Soil Sci. **63**, 848–860 (2012).
3. J. M. Soriano-Disla, L. J. Janik, R. A. V. Rossel, L. M. Macdonald, and M. J. McLaughlin, "The performance of visible, near-, and mid-infrared reflectance spectroscopy for prediction of soil physical, chemical, and biological properties," Appl. Spectrosc. Rev. **49**, 139–186 (2014).
4. S. Rodd-Routley, "Refractively scanned interferometer," Patent Cooperation Treaty Application PCT/AU2019/051327 (December 4, 2019); Provisional Australian Patent AU2018904607 filed December 4, 2018.
5. J. P. Dybwad, "Refractively scanned interferometer," U.S. Patent 4,654,530 (March 31, 1987).
6. W. Wadsworth and J.-P. Dybwad, "Rugged high-speed rotary imaging Fourier transform spectrometer for industrial use," Proc. SPIE **4577**, 83–88 (2002).
7. Y.-M. Lee, M. Toda, M. Esashi, and T. Ono, "Micro wishbone interferometer for Fourier transform infrared spectrometry," J. Micromech. Microeng. **21**, 065039 (2011).
8. "Introduction to FTIR spectroscopy," Tech. Rep., Newport Corporation, 2020, https://www.newport.com/n/introduction-to-ftir-spectroscopy.
9. M. Born and E. Wolf, *Principles of Optics: Electromagnetic Theory of Propagation, Interference and Diffraction of Light* (Cambridge University, 2000).
10. J. L. Synge, "Hamilton's method in geometrical optics," J. Opt. Soc. Am. **27**, 75–82 (1937).
11. H. Buchdahl, *An Introduction to Hamiltonian Optics*, Dover Classics of Science and Mathematics (Dover, 1993).
12. M. A. Alonso and G. W. Forbes, "Generalization of Hamilton's formalism for geometrical optics," J. Opt. Soc. Am. A **12**, 2744–2752 (1995).
13. W. Shen, J. Zhang, S. Wang, and S. Zhu, "Fermat's principle, the general eikonal equation, and space geometry in a static anisotropic medium," J. Opt. Soc. Am. A **14**, 2850–2854 (1997).
14. A. L. Rivera, S. M. Chumakov, and K. B. Wolf, "Hamiltonian foundation of geometrical anisotropic optics," J. Opt. Soc. Am. A **12**, 1380–1389 (1995).
15. D. D. Holm and K. Wolf, "Lie-Poisson description of Hamiltonian ray optics," Physica D **51**, 189–199 (1991).
16. A. J. Dragt, "Lie algebraic theory of geometrical optics and optical aberrations," J. Opt. Soc. Am. **72**, 372–379 (1982).